Applied Catalysis B: Environmental 220 (2018) 303–313

Contents lists available at ScienceDirect

Applied Catalysis B: Environmental

journal homepage: www.elsevier.com/locate/apcatb

Sub 1 nm aggregation-free AuPd nanocatalysts confined inside amino-functionalized organosilica nanotubes for visible-light-driven hydrogen evolution from formaldehyde

Shengbo Zhang[a,1], Hua Wang[a,1], Lei Tang[a], Mei Li[a], Jianhang Tian[a], Yue Cui[a], Jinyu Han[a], Xinli Zhu[a], Xiao Liu[a,b,*]

[a] Key Laboratory for Green Chemical Technology of the Ministry of Education, School of Chemical Engineering and Technology, Tianjin University, Tianjin 300072, PR China

[b] Key Laboratory of Pesticide & Chemical Biology of the Ministry of Education, College of Chemistry, Central China Normal University, Wuhan 430079, PR China

ARTICLE INFO

Keywords:
Amino-functionalized
Organosilica nanotubes
AuPd alloy
Photocatalytic hydrogen evolution
Formaldehyde

ABSTRACT

Novel amino-functionalized organosilica nanotubes (AM-NT) were facilely synthesized by the hydrolysis and co-condensation of 3-aminopropyltrimethoxysilane (APTMS) with 1,4-bis(triethoxysilyl)benzene (BTEB) using a simple micelle-templating approach. Through adjusting the ratios of organosilane precursors, the very short AM-NT with ~60 nm in length and ~6 nm in pore diameter could be controllably obtained. By using the unique AM-NT as the supports, a series of AuPd alloy nanoparticles with the average size of sub 1 nm could be synthesized after the liquid phase reduction of $HAuCl_4$ and H_2PdCl_4 in water, which were mostly confined inside the short organosilica nanotubes and further applied for the hydrogen evolution from formaldehyde aqueous solution. These bimetallic AuPd nanocatalysts in the organic-modified nanotubes exhibited remarkably improved catalytic activity under visible light irradiation and the highest initial TOF value of 241.7 h^{-1} could be achieved at the room temperature. Furthermore, these ultrasmall nanocatalysts exhibited high reaction stability and no aggregation of metal nanoparticles was observed even after 5 recycles. The superior catalytic activity was mainly attributed to the uniform and ultrafine AuPd nanostructure, benefiting from the synergetic stabilizing effects of amino and benzene groups in the nanotube frameworks. The fast electron transfer from much smaller Au with localized surface plasmon resonance (LSPR) to active Pd sites could efficiently occur, resulting in the excellent photocatalytic activity.

1. Introduction

Hydrogen is widely utilized in the petroleum and chemical industries, such as the upgrading of fossil fuels, ammonia production and proton exchange membrane fuel cells (PEMFC), which may play a vital role in the future to satisfy the energy demand [1–6]. Most of the hydrogen employed today in industry is supplied from coal gasification and steam reforming, leading to the continuous consumption of limited fossil resources. Moreover, the controllable storage and safe delivery of hydrogen still restrict its widespread application. From the point of view of sustainable development, it is highly desirable to explore more mild and maneuverable manners for hydrogen production using alternative technologies. Recently, the hydrogen evolution from liquid-phase chemical hydrogen storage materials, such as formic acid [7–14], methanol [15,16], sodium borohydride [17–19], ammonia borane [20,21], and formaldehyde [22–25] has been attracted much research attention and intensively studied. Among them, the reduction of formaldehyde (HCHO) to H_2 using water as one of the hydrogen donors ($HCHO + H_2O \rightarrow HCOOH + H_2$) can be considered as an efficient and promising hydrogen generation strategy due to its atomic economy and nonflammable hydrogen carrier of formaldehyde. More importantly, the resulting gas is only pure hydrogen without CO or CO_2 generation in alkaline solutions, which can greatly meet the criteria of hydrogen production from cost, safety and purity, especially for PEMFC.

Many studies have confirmed that some metal nanoparticles can act as catalysts and significantly accelerate the hydrogen evolution rate from formaldehyde alkaline solution, such as monometallic Cu [26], Pt [27], Ag [25,28], Ni [26], Au [29] and bimetallic AgPd alloy [30].

* Corresponding author at: Key Laboratory for Green Chemical Technology of the Ministry of Education, School of Chemical Engineering and Technology, Tianjin University, Tianjin 300072, PR China.
E-mail address: liuxiao71@tju.edu.cn (X. Liu).
[1] These authors contributed equally.

http://dx.doi.org/10.1016/j.apcatb.2017.08.043
Received 29 June 2017; Received in revised form 11 August 2017; Accepted 14 August 2017
Available online 19 August 2017
0926-3373/

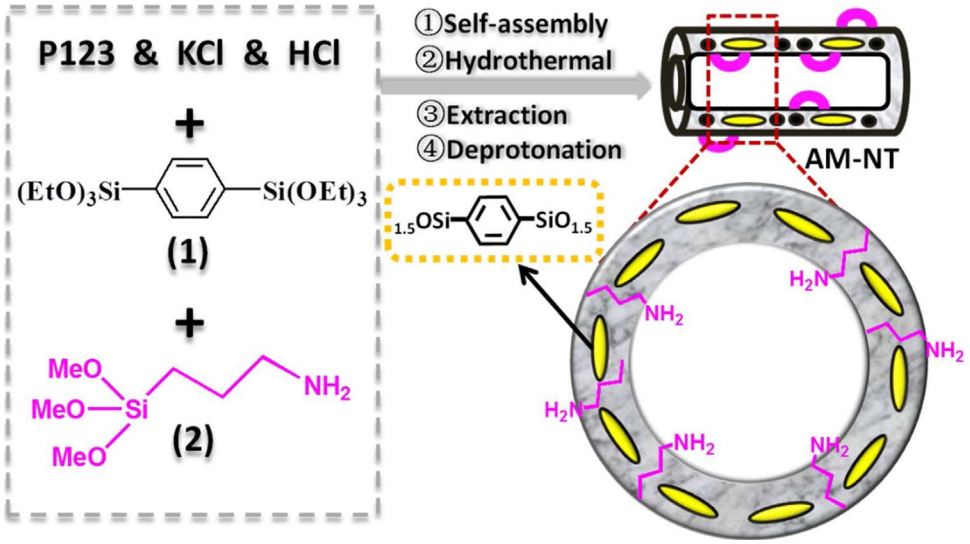

Scheme 1. Synthetic routes of amine- incorporated organosilica nanotubes.

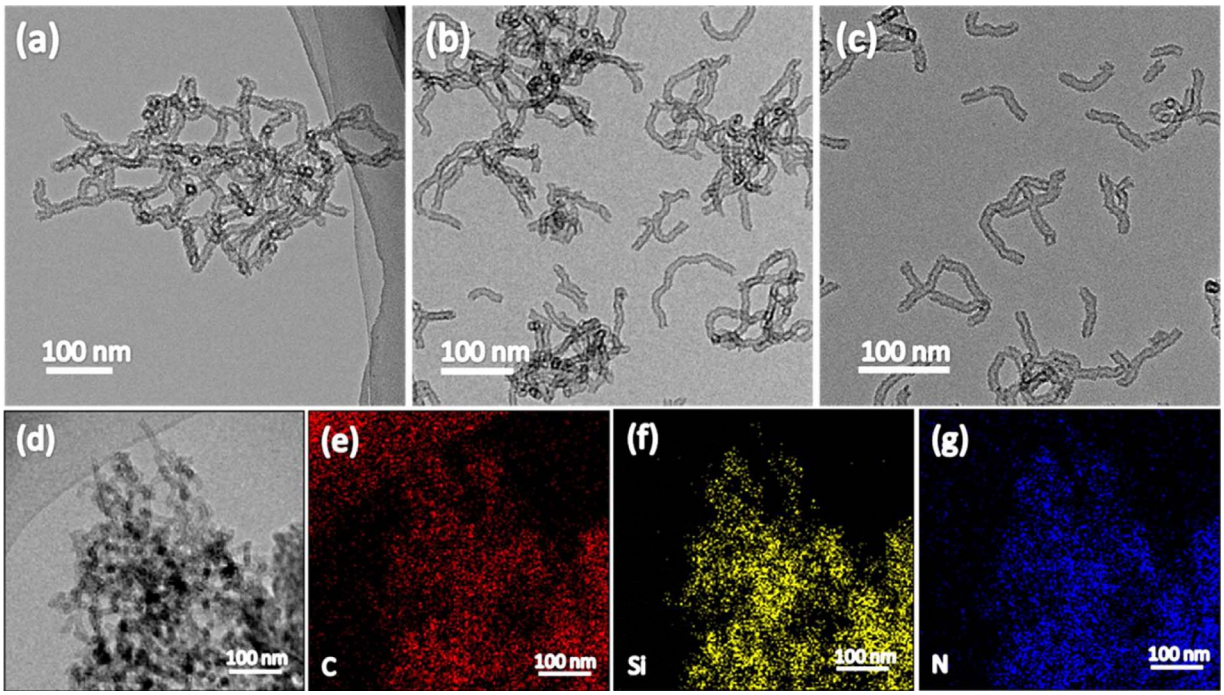

Fig. 1. The TEM images of (a) $AM_{0.1}$-NT, (b) $AM_{0.2}$-NT, (c) $AM_{0.4}$-NT. (d) Dark field STEM image and (e-g) the elemental mapping images of $AM_{0.4}$-NT.

Especially, ultrasmall metal nanoparticles are of great interest due to their unique nanostructure-dependent properties, such as high dispersion, high surface-to-atom ratio, abundant edge and corner atoms and quantum confinement effects, which drastically differentiate their catalytic performance from that of bulk metals [7–9,31–39]. However, using small metal nanoparticle as catalysts suffers from one fatal drawback: small metal nanoparticles tend to aggregate or coalesce owing to their low Tammann temperatures and high surface energies, which seriously makes the active sites and catalytic performance decrease. Therefore, it still remains a challenge for the synthesis of well-dispersed and ultrafine metal nanoparticles with high activity and stability. On the other hand, the hydrogen evolution from alkaline formaldehyde solution has also been achieved from semiconductors under visible light irradiation [40,41]. However, as far as we know, there is no any report about the Au- or Ag-containing bimetallic alloys for visible-light-driven hydrogen evolution from formaldehyde, in the utilization of the localized surface plasmon resonance effect of Au or Ag.

Organosilica nanotubes containing various organic functionalities in the frameworks are a new kind of organic-inorganic hybrid mesoporous material, which possess the distinct properties such as robust nanostructure, high surface areas, large channel structure and tunable hydrophilicity/hydrophobicity [42–46]. Our previous study has demonstrated that the organic groups in the frameworks could facilitate the formation of smaller metal nanopartlces to enhance the reaction activity [42,47]. Considering the much stronger stabilizing effect of amino groups for metal nanoparticles, herein, we report the synthesis of benzene-bridged organosilica nanotubes containing amino groups in the framework and its encapsulation of AuPd alloys in the nanotube channels. Interestingly, the very short amino-incorporated organosilica nanotubes with ~60 nm in length and pore diameter of ~6 nm could be controllably synthesized. A series of well-dispersed and ultrafine AuPd nanoparticles supported on cut-shorted organosilica nanotubes were successfully obtained and applied for the hydrogen evolution from

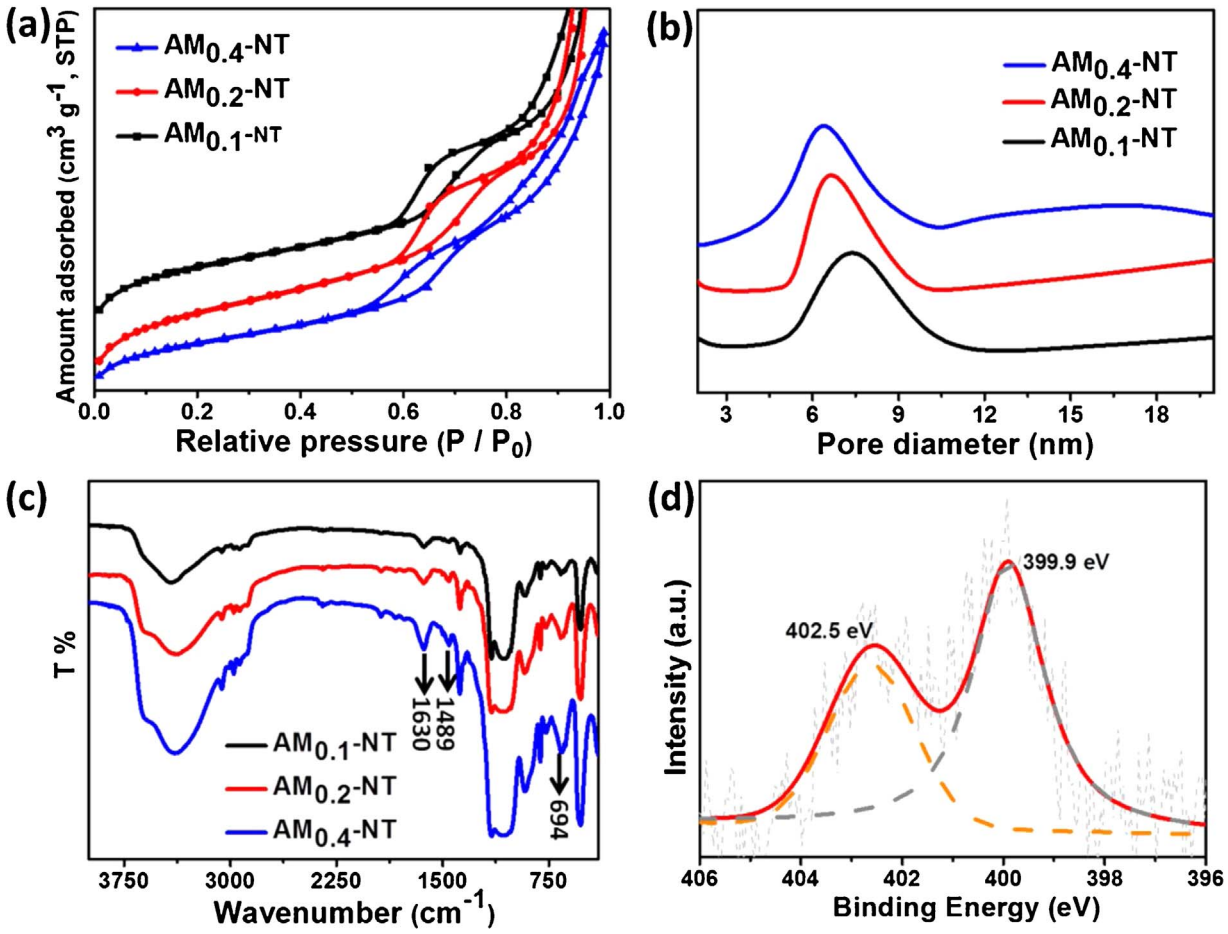

Fig. 2. (a) Nitrogen adsorption-desorption isotherms of AM_x-NT, (b) Pore size distributions of AM_x-NT, (c) FT-IR spectra of AM_x-NT and (d) The XPS N1 s spectrum of $AM_{0.4}$-NT.

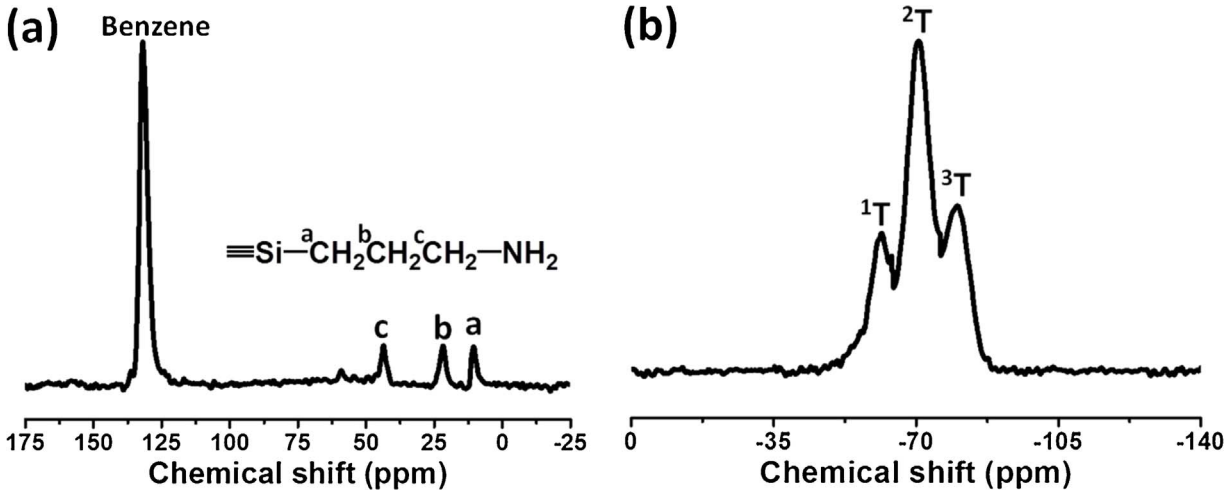

Fig. 3. (a) ^{13}C CP MAS NMR spectrum and (b) ^{29}Si MAS NMR spectrum of the $AM_{0.4}$-NT.

formaldehyde aqueous solution at room temperature. These catalysts with different molar ratios of Au/Pd exhibited remarkably enhanced catalytic activity under visible light irradiation than that in the dark. The highest photocatalytic activity with an initial TOF value of 241.7 h^{-1} was obtained at room temperature. The superior catalytic activity was mainly attributed to the ultrafine AuPd nanostructure and the efficient electron transfer from Au clusters with localized surface plasmon resonance (LSPR) effect to active Pd sites [11,20,48–52]. What's more, the heterogeneous nanotube catalysts exhibited the significantly improved recyclability owing to the highly robust nanostructure and the effective suppression of active sites aggregation.

2. Experimental

2.1. Materials

Triblock copolymer $EO_{20}PO_{70}EO_{20}$ (Pluronic P123, Mw = 5800), 1,4-bis(triethoxysilyl)benzene (BTEB) were purchased from Sigma-Aldrich Company Ltd. (U.S.A.). 3-aminopropyltrimethoxysilane (97%) was obtianed from *J & K*. Other reagents (KCl, $NaBH_4$, $HAuCl_4$, $PdCl_2$)

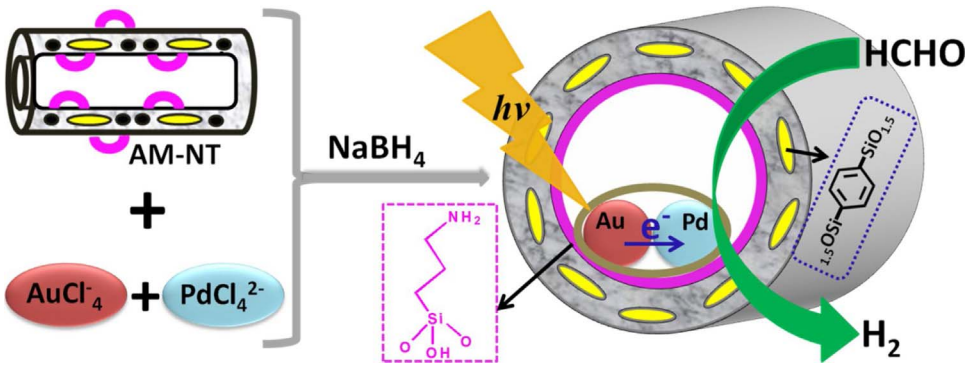

Scheme 2. Synthetic routes and photocatalytic hydrogen evolution of amino-functionalized organosilica nanotubes supported AuPd alloy nanoparticles.

Table 1
Physicochemical properties of different materials.

Catalysts	S_{BET}[a] (m^2/g)	Pore diameter[b] (nm)	Particle size (nm)	Au[c] (wt%)	Pd[c] (wt%)	AuPd Final composition (mol/mol)
$Au/AM_{0.4}$-NT	675	6.3	0.9 ± 0.2	4.60	–	1:0
$Au_4Pd_1/AM_{0.4}$-NT	663	6.2	0.7 ± 0.3	3.75	0.54	3.92:1
$Au_1Pd_1/AM_{0.4}$-NT	672	6.3	0.8 ± 0.2	2.40	1.31	1:1.02
$Au_1Pd_4/AM_{0.4}$-NT	649	6.1	0.8 ± 0.2	0.96	2.08	1:4.06
$Pd/AM_{0.4}$-NT	657	6.2	1.0 ± 0.3	–	2.57	0:1
Au_1Pd_4/NT	710	6.8	3.0 ± 1.0	0.98	2.11	1:3.98

[a] The BET surface areas were calculated using the data in the relative pressure range of P/P_0 = 0.05–0.25.
[b] Pore size distributions were calculated from adsorption branch using the BJH method.
[c] The ICP-AES results.

were purchased from Shanghai Chemical Reagent. All solvents were of analytical grade and used as received without any further purification.

2.2. Synthesis of amino-functionalized organosilica nanotubes

In a typical synthesis, 0.55 g of P123 and 1.75 g of KCl were dissolved in 150 mL of 2 M HCl solution at 38 °C. After stirring for 2 h at 38 °C, 2.1 mmol of 1, 4-bis(triethoxysilyl)benzene (BTEB) (1) was added with vigorous stirring. After stirring for 12 h at 38 °C, 1.4 mmol of 3-aminopropyltrimethoxysilane (APTMS) (2) was added dropwise. The molar ratio of APTMS in the resulting mixture was 0.4. After the mixture was stirred at 38 °C for 24 h, the resultant mixture was transferred to a PTFE hydrothermal reactor for an additional 24 h at 100 °C. The solid product was recovered by filtration and was dried. Finally, the surfactant was extracted by refluxing in acid-ethanol solution for 24 h. The obtained sample was denoted $AM_{0.4}$-NT. Similarly, the AM-NT with molar ratio of APTMS of 0.1 and 0.2 were also synthesized, denoted as $AM_{0.1}$-NT and $AM_{0.2}$-NT, respectively.

2.3. Synthesis of AuPd supported on $AM_{0.4}$-NT

For preparation of $AuPd/AM_{0.4}$-NT, 100 mg $AM_{0.4}$-NT was dispersed in 30 mL water, then $HAuCl_4$ and H_2PdCl_4 (mole ratio = 1:0, 4:1, 1:1, 1:4, 0:1) was added, and then stirred for 24 h at room temperature. Then 2 mL 1.0 M $NaBH_4$ was added and stirred for 4 h. The mixture was filtered, washed and dried at room temperature. The obtained samples were denoted $Au/AM_{0.4}$-NT, $Au_4Pd_1/AM_{0.4}$-NT, $Au_1Pd_1/AM_{0.4}$-NT, $Au_1Pd_4/AM_{0.4}$-NT and $Pd/AM_{0.4}$-NT, respectively.

2.4. Characterization

Transmission electron microscopys (TEM) were operated on a JEM-2100F system operating at 200 kV. Powder X-ray diffraction (XRD) patterns were performed on a Rigaku D/MAX-2500 diffractometer at room temperature conditions using a filtered Cu-Kα radiation source (λ = 1.54056 Å). The test range were operated from 30° to 90° (2θ) at a scanning speed of 5°/min. N_2 adsorption-desorption isotherms were tested at −196 °C on a Micromeritics Tristar 3000 instrument. The specific surface area was obtained by the Brunauer–Emmett–Teller method; the pore size distribution was obtained by the Barrett–Joyner–Halenda method using the adsorption branch. X-ray photoelectron spectroscopy (XPS) was carried out on a PHI 1600 (PerkinElmer). All spectra were recorded at room temperature and the binding energy was referred to C 1 s peak at 284.8 eV. UV/vis absorption and diffuse reflectance spectra were obtained using Instant Spec BWS003 spectrometers. FT-IR spectra were collected with a Bruker Vertex 80 v. Carbon, hydrogen and nitrogen contents were determined via CHN elemental analysis. Solid-state ^{13}C cross polarization magic-angle spinning (CP MAS) NMR and ^{29}Si magic angle spinning (MAS) NMR spectra were collected on 400 MHz instruments.

2.5. Hydrogen evolution from formaldehyde

In a typical experiment, $AuPd/AM_{0.4}$-NT (0.04 mmol AuPd) was added to a fresh HCHO and NaOH solution (100 mL) after being purged with N_2 for 0.5 h. The reaction was operated at room temperature with a visible light (λ > 420 nm) illumination. The H_2 molecules generated in the head space were periodically analyzed quantitatively by a Bruker 456 gas chromatograph equipped with a thermal conductivity detector (TCD). For the recycling catalytic performance, after every 1 h, the catalyst was recovered by simple filtration, dried and used for the next reaction.

3. Results and discussions

3.1. Synthesis of amino-functionalized organosilica nanotubes (AM_x-NT)

The amino-functionalized organosilica nanotubes were synthesized by the hydrolysis and co-condensation of 1,4-bis(triethoxysilyl)benzene (BTEB) (1) and 3-aminopropyltrimethoxysilane (APTMS) (2) under acid conditions using triblockcopolymer $[(EO)_{20}(PO)_{70}(EO)_{20}$, P123] as a soft template, followed by the extraction of template agent with an acidic ethanol solution and deprotonation of the amino groups by stirring the extracted samples in 0.01 M NaOH aqueous solution. The

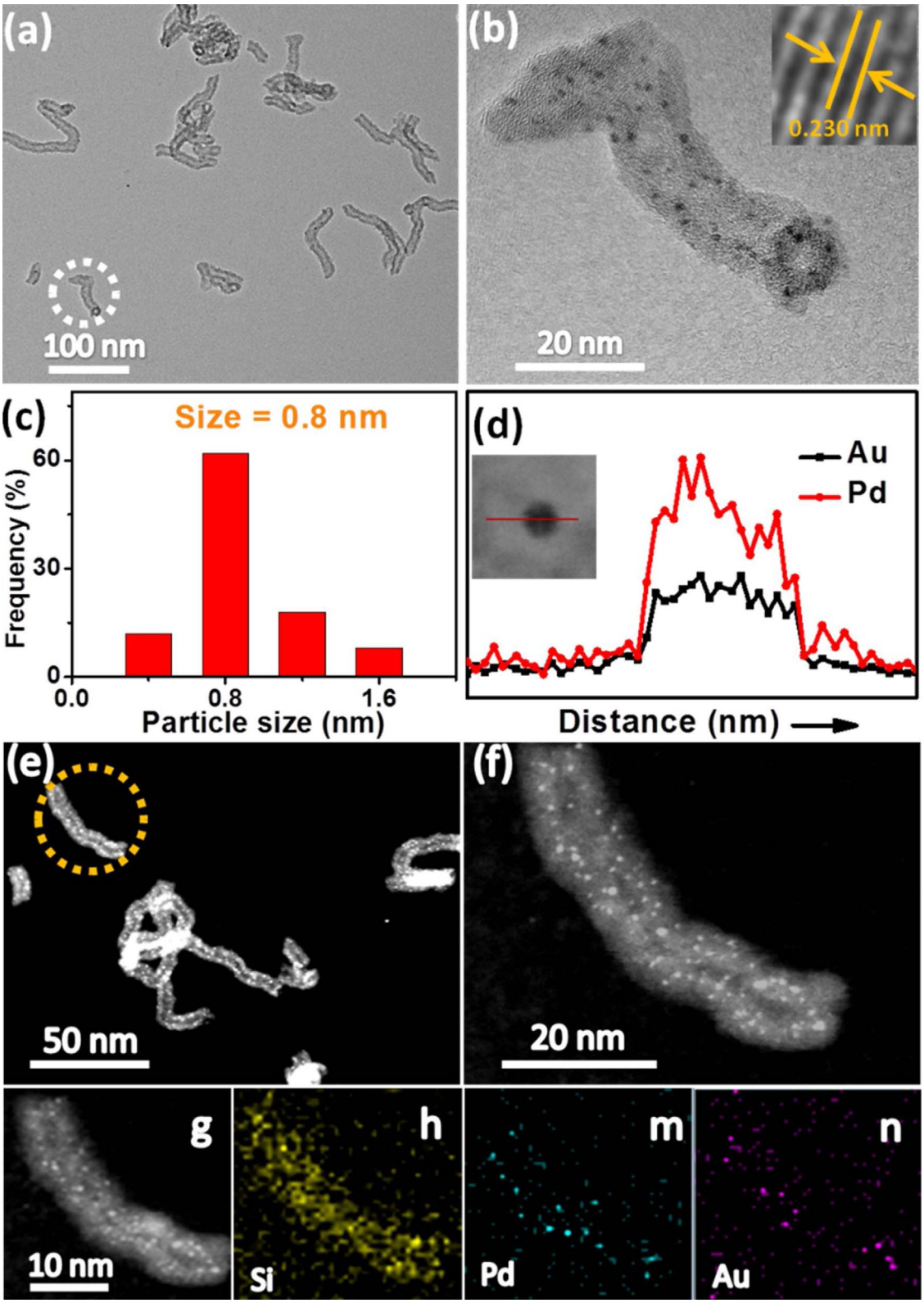

Fig. 4. (a, b) The TEM images, (c) particle size distribution of Au_1Pd_4, (d) the line-scanning analysis for Au and Pd, (e-g) HAADF-STEM, and (h-n) the corresponding elemental mapping images of $Au_1Pd_4/AM_{0.4}$-NT.

final sample were denoted as AM_x-NT [x = 0.1, 0.2 and 0.4, respectively, responding to the molar ratio of APTMS in the initial silane mixture] (Scheme 1).

Fig. 1a–c shows the transmission electron microscopy (TEM) images of AM_x-NT, which clearly manifest that the obtained materials are composed of nanotube with the inner diameter of ~6 nm and wall thickness of ~3 nm. We also note that the nanotubes could be cut short by the adjustment of the molar ratio of APTMS in the synthetic process. When the molar ratio was 0.2, some short nanotubes appeared with the length of ~100 nm (Fig. 1b). With the continuous increasing of the

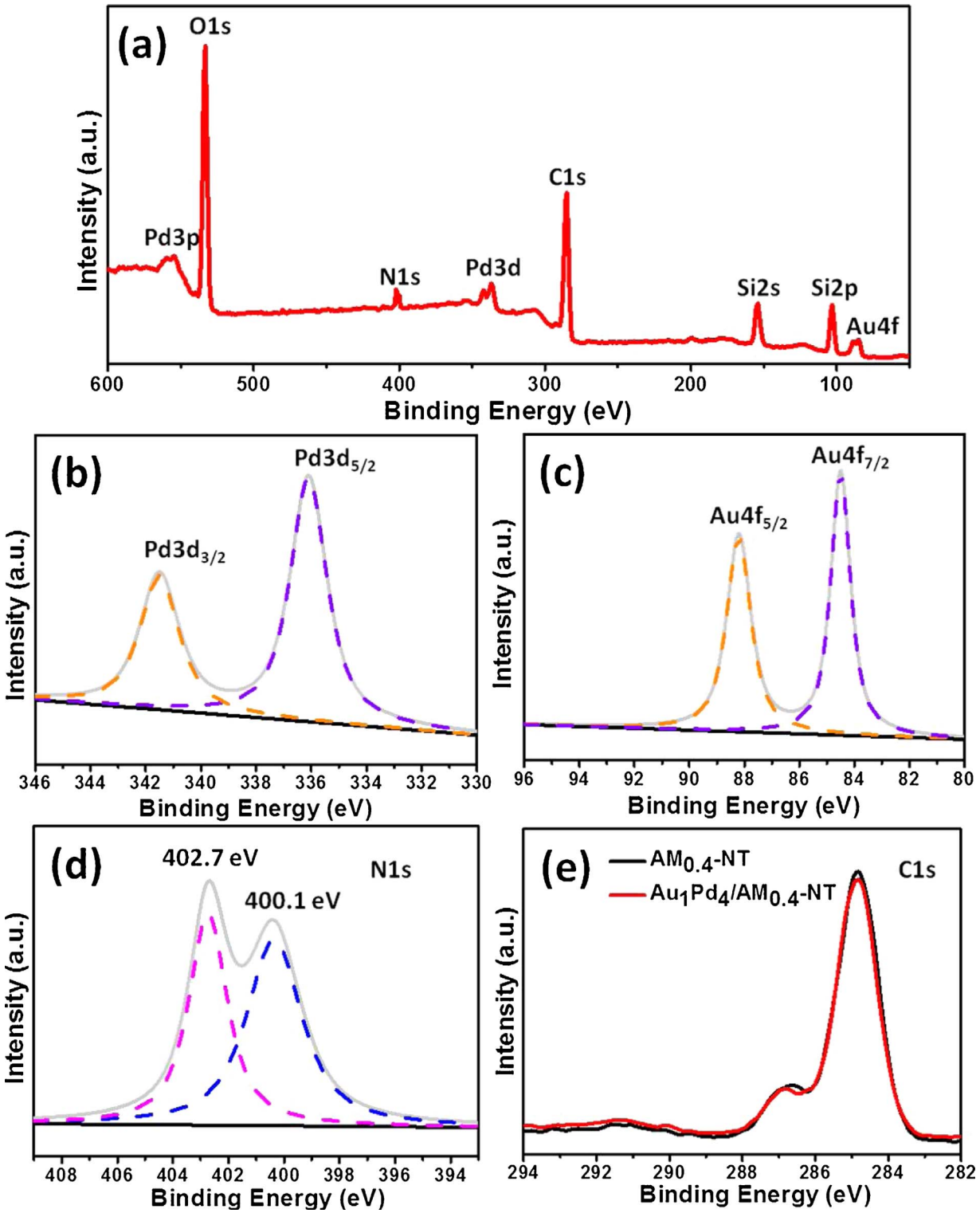

Fig. 5. (a) The XPS of $Au_1Pd_4/AM_{0.4}$-NT, (b) the XPS of Pd 3d regions, (c) the XPS of Au 4f regions, (d) the XPS of N 1 s regions of $Au_1Pd_4/AM_{0.4}$-NT and (e) the XPS of C 1 s regions of $Au_1Pd_4/AM_{0.4}$-NT and $AM_{0.4}$-NT.

ratio to 0.4, uniform short nanotubes were obtained with the length in the range of 40–100 nm. In order to know the locations of amino groups in the nanotubes, the energy-dispersive X-ray spectrometry (EDX) mapping analysis for $AM_{0.4}$-NT was conducted (Fig. 1d-g). The uniform distribution of N in the chosen area indicates that NH_2 group was uniformly distributed on the nanotube support. In addition, the N loadings of $AM_{0.1}$-NT, $AM_{0.2}$-NT and $AM_{0.4}$-NT were 0.22, 0.48 and 1.03 mmol/g by the CHN elemental analysis.

The nitrogen adsorption-desorption isotherms of the AM_x-NT were type IV with a hysteresis loops at relative pressures P/P_0 = 0.5-0.7, which is typical for mesoporous materials (Fig. 2a). The pore diameter and BET surface areas were found to be slightly decreased following the increase of the molar ratio of aminosilane precursors in the synthetic process, as shown in Fig. 2b, Table S1. These phenomena can be attributed to more amino groups functionalized inside the channels of the nanotubes, leading to the shrinkage of the channels. Fig. 2c shows the

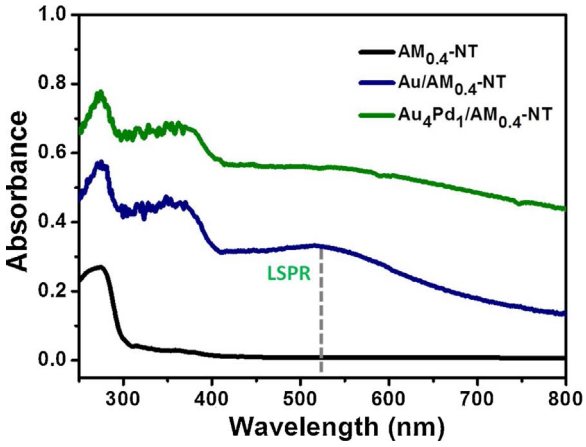

Fig. 6. UV-vis spectra of $AM_{0.4}$-NT and AuPd/$AM_{0.4}$-NT materials.

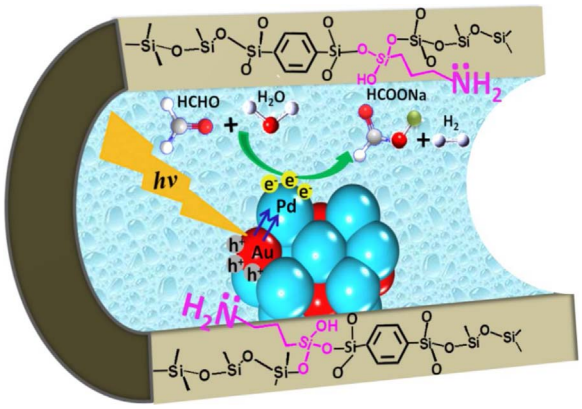

Scheme 3. Schematic illustration of photocatalytic hydrogen evolution from formaldehyde for $Au_1Pd_4/AM_{0.4}$-NT.

FT-IR spectra of organosilica nanotubes with different amino contents. The bands at 1150 cm^{-1}, 1300–2000 cm^{-1} and 3035 cm^{-1} correspond to the Si-C vibrations, benzene ring vibrations and the stretching modes of C-H species of aromatic moiety, respectively. The peaks at 694 cm^{-1} and 1630 cm^{-1} were ascribed to the N-H bending vibration. Additionally, the peak at 1489 cm^{-1} was assigned to C-H vibration of CH_2 in $SiCH_2CH_2CH_2NH_2$ from APTMS. What's more, the N1 s X-ray photoelectron spectroscopy (XPS) of $AM_{0.4}$-NT was tested and shown in Fig. 2d. The peaks at 399.6 and 402.5 eV can be ascribed to the nitrogen atoms in the $-NH_2$ and $-NH_3^+$, respectively, which indicate that nitrogen atoms are mainly in $-NH_2$ form.

The solid-state ^{13}C cross polarization magic-angle spinning (CP MAS) NMR spectrum of $AM_{0.4}$-NT (Fig. 3a) exhibited a strong peak at 133 ppm, which belonged to benzene group from 1,4-bis(triethoxysilyl) benzene (BTEB). The peaks at 10, 21.5 and 43 ppm were assigned to alkyl $SiCH_2CH_2CH_2NH_2$ groups from aminosilane APTMS. The signals at 58 ppm were due to the carbons of the ethoxy groups formed during the ethanol treatment for removal of the surfactant. The ^{29}Si magic angle spinning (MAS) NMR spectrum of $AM_{0.4}$-NT (Fig. 3b) showed three resonance peaks at −62, −71, −80 ppm, which were assigned to silicon species ^1T [$SiC(OH)_2(OSi)$], ^2T [$SiC(OH)(OSi)_2$] and ^3T [$SiC(OSi)_3$], respectively. The above results fully indicate the successful synthesis of amino-functionalized organosilica nanotubes. More importantly, the nanotube length could be easily controllable through the adjustment of precursor ratios during the synthesis, which has not been reported previously for amino-functionalized nanotubes.

3.2. Synthesis of bimetallic Au–Pd nanoparticles on amino-functionalized organosilica nanotubes

Subsequently, using unique short amino-functionalized organosilica nanotubes as the supprots, a series of bimetallic Au-Pd nanoparticles were prepared by the co-reduction method of $HAuCl_4$ and H_2PdCl_4 with $NaBH_4$ as reductant (Scheme 2). The mole ratio of Au to Pd was adjusted by changing that of $HAuCl_4$ and H_2PdCl_4 to 1:0, 4:1, 1:1, 1:4, 0:1, respectively. The final samples were denoted as Au/$AM_{0.4}$-NT, Au_4Pd_1/$AM_{0.4}$-NT, $Au_1Pd_1/AM_{0.4}$-NT, $Au_1Pd_4/AM_{0.4}$-NT, Pd/$AM_{0.4}$-NT and the compositions of AuPd alloy were analyzed by Inductively Coupled Plasma-Atomic Emission Spectroscopy (ICP-AES), which is very close to the theoretical results (Table 1).

The TEM images of the as-prepared Au, Pd and AuPd show that almost all the nanoparticles are homogeneously distributed on the surface of amino-functionalized organosilica nanotubes with an ultrafine size distribution (Fig. 4a,b, Fig. S1, Table 1). For example, the average size of Au_1Pd_4 on $AM_{0.4}$-NT is only about 0.8 nm (Fig. 4c), composed of several Au and Pd atoms. It should be noted that such size is much smaller than that of metal nanoparticles supported on amino-functionalized pure SiO_2 materials (2–5 nm) [53–55] or on only benzene-incorporated organosilica nanotubes without amino groups (Fig. S10). The well-dispersed and ultrafine AuPd nanoparticles in Au_1Pd_4/$AM_{0.4}$-NT may be due to the synergistic stabilization effect of amino and benzene ring in the network of organosilica nanotubes [9,42,47,53–59]. A lattice fringe of 0.230 nm between those of the (111) planes of fcc Au (0.236 nm) and fcc Pd (0.227 nm) is observed in the HRTEM of $Au_1Pd_4/AM_{0.4}$-NT (Fig. 4b inserted), indicating the formation of the AuPd alloy. In addition, the formation of AuPd alloy structure was also further confirmed by the line-scan EDX analysis (Fig. 4d). In order to further study the distribution and location of AuPd nanoparticles on the nanotubes, the high-angle-annular-dark-field scanning transmission electron microscopy (HAADF-STEM) (Fig. 4e-g) and energy-dispersive X-ray spectroscopy (EDS) elemental mapping (Fig. 4h-n) were implemented. From the results we can see that most of the AuPd nanoparticles were homogeneously distributed on the inner surface of nanotubes, not outside. The elemental mapping of Au_1Pd_4/$AM_{0.4}$-NT from EDS shows that the Au and Pd are dispersed in the alloys with a slightly larger Pd map area than that of Au, which is in good agreement with the ratio of metals. These above results indicate that the successful formation of well-dispersed and ultrafine AuPd nanoparticles, benefiting from the synergistic stabilizing effect of the amino and benzene ring in the network of organosilica nanotubes.

X-ray photoelectron spectroscopy (XPS) analysis was carried out to test the electronic states of different elements in $Au_1Pd_4/AM_{0.4}$-NT (Fig. 5a). In the Pd 3d spectrum (Fig. 5b), the $3d_{5/2}$ and $3d_{3/2}$ peak of Pd^0 appear at 335.4 eV and 340.7 eV, respectively. Compared with that of monometallic Pd 3d (335.8 and 340.8 eV) [54,60], the binding energy for Pd 3d is shifted to a lower value. For the Au 4f spectrum (Fig. 5c), the $4f_{7/2}$ and $4f_{5/2}$ peak of Au^0 appear at 84.5 eV and 88.1 eV, corresponding to a higher binding energy than that of monometallic Au 4f (84.0 and 87.6 eV) [54,60]. These shifts are attributed to the strong interactions between Au and Pd metal in the AuPd alloy and some electrons transfer from Au with localized surface plasmon resonance (LSPR) effect to Pd sites. What's more, the binding energy of N 1 s peak for $Au_1Pd_4/AM_{0.4}$-NT has also a upshift of ~0.2 eV (Fig. 5d) compared with that in $AM_{0.4}$-NT (Fig. 2d), because of the electron-donating properties of amino group and some electrons transfer to Pd sites [9,11,53,59]. Interestingly, the C 1s peak of $Au_1Pd_4/AM_{0.4}$-NT has also slight shifts in comparison with that of $AM_{0.4}$-NT (Fig. 5e), which is possibly due to the interactions between AuPd alloy and benzene rings in the nanotube frameworks. These results further verified the speculation that the synergistic stabilizing effects of amino and benzene groups in the nanotube frameworks helped the formation of well-dispersed and ultrafine AuPd nanoclusters.

The photo absorption properties of Au and AuPd nanoparticles on

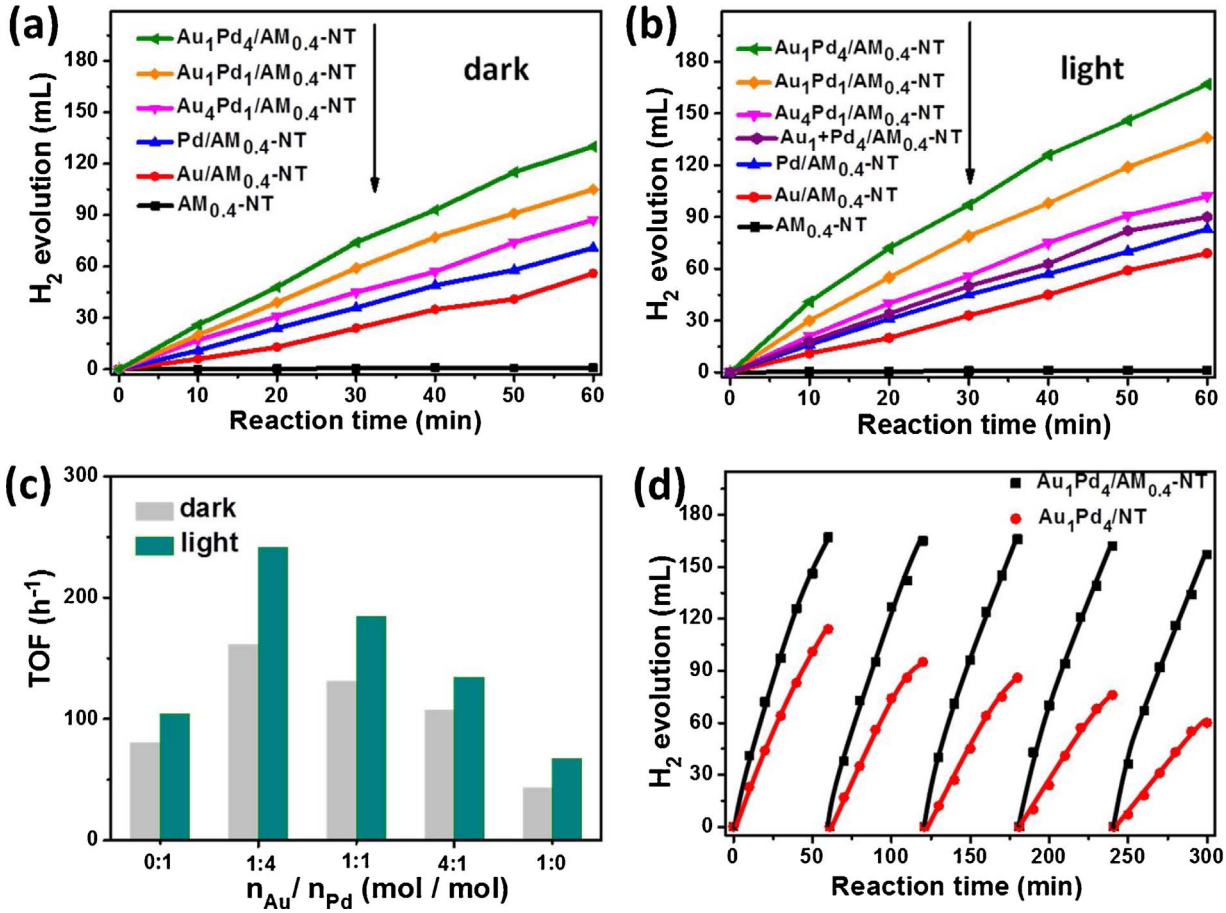

Fig. 7. Time-dependent hydrogen evolution curves from alkaline formaldehyde of all the as-prepared materials (a) in the dark at 298 K and (b) under visible light irradiation (λ > 420 nm) at 298 K. (c) The TOFs of different catalysts in the dark and under visible light irradiation [TOF was calculated from the data within the first 20 min according to the following equation: TOF = $mmol_{hydrogenproduced}/(mmol_{AuPd} \times h)$]. (d) The recycling performance of $Au_1Pd_4/AM_{0.4}$-NT and Au_1Pd_4/NT for hydrogen evolution from formaldehyde under visible light irradiation (λ > 420 nm).

Table 2
Comparison of the catalyst properties during hydrogen evolution from formaldehyde reaction.[a]

Entry	Catalysts	H_2 volume/mL		TOF/h^{-1}		References
		In dark	Light	In dark	Light	
1	$Au/AM_{0.4}$-NT	56	69	43.6	67.1	this
2	$Pd/AM_{0.4}$-NT	71	83	80.6	104.0	work
3	$Au_4Pd_1/AM_{0.4}$-NT	87	102	107.4	134.3	
4	$Au_1Pd_1/AM_{0.4}$-NT	105	136	130.9	184.6	
5	$Au_1Pd_4/AM_{0.4}$-NT	130	167	161.1	241.7	
6	Au_1 + $Pd_4/AM_{0.4}$-NT	–	90	–	114.1	
7	Au_1Pd_4/NT	–	114	–	147.7	
8	$Au_1Pd_4/AM_{0.1}$-NT	–	143	–	194.7	
9	Pd NPs	40[b]		26.5		[23]
10	Pd/TiO_2	100[c]		71.0		[24]
11	Au NPs	25.9[b]		13.7		[26]
12	Cu NPs	29.5[b]		9.8		[26]

[a] Unless other statements, the reaction was carried out under N_2 atmosphere, room temperature and the reaction time was 1 h.
[b] Reaction time was 1.67 h.
[c] Reaction time was 0.5 h. TOF was calculated from the data within the first 20 min according to the following equation: TOF = $mmol_{hydrogenproduced}/(mmol_{AuPd} \times h)$.

$AM_{0.4}$-NT were studied by the UV/vis diffuse reflectance spectrometry (Fig. 6). The organosilica nanotube support $AM_{0.4}$-NT did not contribute to any visible light absorption. In contrast, the Au and Au_4Pd_1 nanoparticles supported on the nanotubes exhibited obvious absorption ability in visible-light region. The characteristic absorption peak at 520 nm due to the LSPR effect of Au nanoparticles could be easily observed [11,20,48,50,52].

3.3. Catalytic performance of $AuPd/AM_{0.4}$-NT catalysts for visible-light-driven hydrogen evolution from formaldehyde

Subsequently, the catalytic hydrogen evolution from alkaline formaldehyde of all the as-prepared $AuPd/AM_{0.4}$-NT samples was tested in a 100 mL 0.3 M formaldehyde solution containing 0.04 mmol AuPd at room temperature. The evolved gas is 100% pure H_2 without CO or CO_2 formation in the reaction system, which was attributed to the decomposition of HCHO and H_2O (Figs. S18, S19, Scheme 3). The time profile plots of hydrogen production are shown in Fig. 7a in the dark condition. It can be seen clearly that there was almost no hydrogen formation using the only organosilica nanotubes without metals. When Au or Pd nanoparticles were immobilized, hydrogen was immediately generated without the induction period and the amount of hydrogen was increased linearly to 56 and 71 mL (Table 2) after one hour for $Au/AM_{0.4}$-NT and $Pd/AM_{0.4}$-NT, respectively. It was found that the catalytic activity of bimetallic AuPd were higher than that of monometallic Au or Pd and $Au_1Pd_4/AM_{0.4}$-NT gave the highest hydrogen amount of about 130 mL under the same conditions (Table 2). The higher activity of AuPd alloys could be attributed to the strong interactions and the alloying synergistic effect between ultrasmall Au and Pd nanoparticles [11,20,21,51–53]. On the other hand, we suppose if light illumination could help the hydrogen evolution from alkaline formaldehyde for AuPd alloys, which has not been reported previously as far as we know.

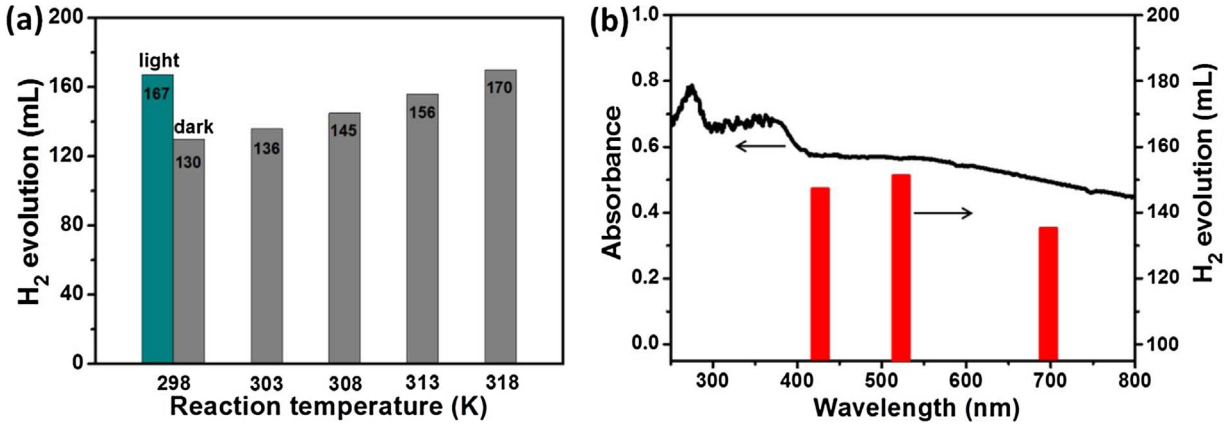

Fig. 8. (a) Effect of the temperature under dark and light irradiation (λ > 420 nm) and (b) Wavelength dependence under monochromatic light irradiation (435, 520, 700 nm) on the hydrogen evolution from formaldehyde for the $Au_1Pd_4/AM_{0.4}$-NT.

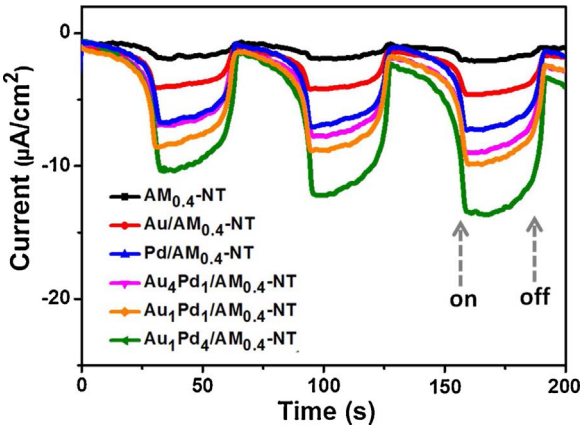

Fig. 9. Transient photocurrent responses of all as-prepared AuPd/$AM_{0.4}$-NT materials.

To our surprise, all the catalysts performed an enhanced activity under visible light irradiation compared to the dark condition (Fig. 7b). $Au_1Pd_4/AM_{0.4}$-NT exhibited the highest activity with a high TOF value of 241.7 h^{-1} and the largest enhancement rate of 0.5 in TOF was obtained under λ > 420 nm visible light irradiation (Fig. 7c, Table 2). About 167 mL hydrogen was generated within one hour for $Au_1Pd_4/AM_{0.4}$-NT, 37 mL higher than that in the dark.

The effect of the temperature on the hydrogen evolution performance from alkaline formaldehyde was carried out in the dark with $Au_1Pd_4/AM_{0.4}$-NT (Fig. 8). With the temperature increasing from 298 to 318 K, the hydrogen amount increased from 130 to 170 mL. Obviously, the catalytic activity under visible light irradiation at 298 K was approximately equal to that in the dark at 318 K and significant higher than that in the dark at 298 K (Fig. 8a). These results suggested that the enhanced activity for $Au_1Pd_4/AM_{0.4}$-NT under visible light irradiation at 298 K was mainly attributed to the light illumination and alloying effect, which has also been evidenced by the previous reports [11,20,21,52,61,62]. Furthermore, the dependence of the light wavelength on the catalytic activity was investigated at 298 K (Fig. 8b). The $Au_1Pd_4/AM_{0.4}$-NT showed higher activity at wavelength of 520 nm than those at 435 nm and 700 nm, which was attributed to the different light absorption and LSPR effect.

In order to know the separation efficiency of the photogenerated charges, the transient photocurrent response results of amino-functionalized organosilica nanotubes supported AuPd alloy nanoparticles with different Au/Pd ratios are shown in Fig. 9. The photocurrent increased immediately when the light irradiation turned on, while the photocurrent quickly decreased when the light was off, demonstrating the existence of the photoresponse for AuPd nanoclusters on nanotubes. Moreover, the photocurrent densities of AuPd/$AM_{0.4}$-NT catalysts are higher than those of Au/$AM_{0.4}$-NT and Pd/$AM_{0.4}$-NT, indicating that the photoinduced electrons and holes on the Au can be rapidly separated and transferred to the Pd surface, which was also evidenced by XPS (Fig. 5). Especially, $Au_1Pd_4/AM_{0.4}$-NT shows the highest photocurrent density of about 12 μA/cm^2, demonstrating the highest photogenerated charge separation and migration from Au to Pd sites. From the above results, the enhanced high activity of AuPd alloys under visible light irradiation than in the dark could be concluded to the

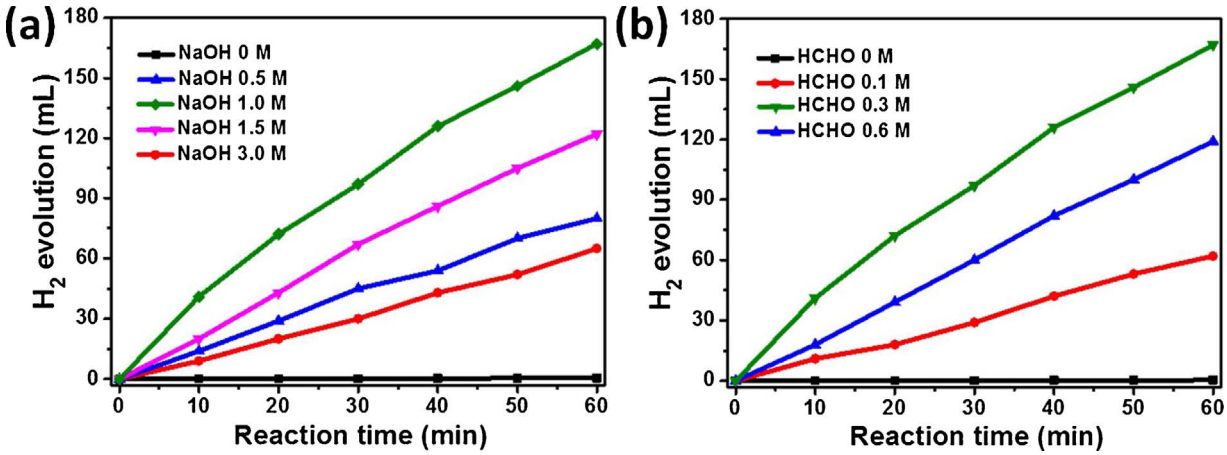

Fig. 10. (a) Effect of NaOH concentration and (b) HCHO concentration on the hydrogen evolution from formaldehyde under visible light irradiation (λ > 420 nm) for the $Au_1Pd_4/AM_{0.4}$-NT.

promotion of the electron of Au excitation and the efficient electron transfer to active Pd sites. The recombination of photoinduced electrons-holes pairs was significantly suppressed, benefiting from the short electron transfer path because of the well-dispersed and ultrafine AuPd alloy nanoclusters (Scheme 3) [11,20,21,52].

For comparison, $Au/AM_{0.4}$-NT and $Pd/AM_{0.4}$-NT were physically mixed on the basis of Au/Pd mole ratio of 1/4 (noted as $Au_1 + Pd_4/AM_{0.4}$-NT) and the reaction activity was shown in Fig. 7b. The hydrogen amount was about 90 ml after one hour under light irridiation with the TOF of 114.1 h^{-1}, much lower than that of $Au_1Pd_4/AM_{0.4}$-NT, demonstrating the acceleration effect of Au_1Pd_4 alloy for the reaction. Furthermore, Au_1Pd_4 alloy was also synthesized on only benzene-incorporated organosilica nanotubes without amino groups (Fig. S9, S10) and long nanotube $AM_{0.1}$-NT (Fig. S20) in order to investigate the effect of the support on the photocatalytic hydrogen production performance. It is interesting to mention that the reaction activity of $Au_1Pd_4/AM_{0.4}$-NT was significantly higher than those of Au_1Pd_4/NT and $Au_1Pd_4/AM_{0.1}$-NT (Fig. S21). The higher activity of $Au_1Pd_4/AM_{0.4}$-NT than Au_1Pd_4/NT and $Au_1Pd_4/AM_{0.1}$-NT could be primarily attributed to the shorter tube length (~60 nm *versus* ~several hundred nm), which can reduce the diffusion limitation and facilitate the fast transport of reactants and products. In addition, amino-functionalized organosilica nanotubes afforded much smaller well-dispersed Au_1Pd_4 particles than that without amino groups (sub 1 nm *versus* ~3 nm), which exhibited higher activity due to the more exposed active sites.

The reusability experiment was then performed at 1 h intervals to investigate the photocatalytic stability of $Au_1Pd_4/AM_{0.4}$-NT under visible light irradiation (Fig. 7d). After the reaction, $Au_1Pd_4/AM_{0.4}$-NT was recovered by simple filtration and reused for the next run. As shown in Fig. 7d, there was no significant decrease in H_2 evolution even after the 5th recycle. After the recyclability, the solid catalyst was removed from the reaction system and was characterized by XRD, TEM, nitrogen adsorption, FT-IR, ^{13}C CP MAS NMR and ^{29}Si MAS NMR (Fig. S23-28). The XRD and TEM images of $Au_1Pd_4/AM_{0.4}$-NT after the 5th reaction exhibited the organosilica nanotube structures without any collapsion and the well-dispersed AuPd nanoparticles without significant aggregation. The nitrogen adsorption-desorption isotherm, FT-IR, ^{13}C CP MAS NMR and ^{29}Si MAS NMR spectra of $Au_1Pd_4/AM_{0.4}$-NT after the 5th reaction further confirmed the intact nanotube structure and the chemical compositions of the frameworks have no change. On the contrast, Au_1Pd_4/NT without amino groups in the nanotubes exhibited the lower recyclability than $Au_1Pd_4/AM_{0.4}$-NT and the activity was gradually decreased (Fig. 7d). TEM image of Au_1Pd_4/NT after the 5th recycle clearly showed the serious aggregation of AuPd alloy in absence of amino functional groups (Fig. S29).

The effects of NaOH and HCHO concentrations on the hydrogen evolution performance were investigated by using the $Au_1Pd_4/AM_{0.4}$-NT catalyst. As shown in Fig. 10a, almost no hydrogen gas was detected in the absence of NaOH. Interestingly, the hydrogen evolution reaction occurred immediately when only a small amount of NaOH was added, indicating that the NaOH is indispensable for this catalytic process. On the other hand, the hydrogen evolution rate for $Au_1Pd_4/AM_{0.4}$-NT catalyst depends largely on the concentration of NaOH. When the concentration of NaOH was increased from 0.5 to 1.0 M, the volume of hydrogen have been increased obviously from 65 to 167 mL at 1 h under the visible light illumination ($\lambda > 420$ nm). However, when further increasing the concentration of NaOH to 1.5 and 3.0 M, the volume of H_2 have been decreased, which attributed to the fact that formaldehyde may be converted into methanol in highly alkaline conditions [23,24]. In addition, the concentration of HCHO has a great influence on hydrogen evolution, as shown in Fig. 10b. It can be seen that the highest reaction activity was obtained at the HCHO concentration of 0.3 M. Therefore, in order to achieve ideal hydrogen evolution performance, the appropriate concentrations of NaOH and HCHO should be controlled reasonably in the reaction process.

4. Conclusions

In summary, the novel cut-shorted robust amino-incorporated organosilica nanotubes with large mesopores have been successfully synthesized under facile conditions. By using the unique amino-functionalized origanosilica nanotubes as the supports, a series of well-dispersed and ultrafine AuPd alloy nanoparticles were designed and prepared. The as-prepared heterogeneous catalysts exhibited superhigh hydrogen evolution performance from formaldehyde aqueous solution under visible light illumination, which was attributed to the ultrafine AuPd alloy nanostructures and the efficient electron transfer from Au with LSPR effect to active Pd sites. To the best of our knowledge, this is the first study of AuPd alloy nanoparticles for hydrogen evolution from formaldehyde aqueous solution under visible light illumination. We believe that this work might open up a new way to obtain H_2 from formaldehyde and provides an integration platform for the heterogeneous catalysis in artificial photosynthesis systems.

Funding

The authors declare no competing financial interest.

Acknowledgments

We thank instrumental analysis centre of Tianjin University for assistance with XRD, TEM, UV/vis, XPS, NMR analysis. We acknowledge the National Natural Science Foundation of China (U1662109), the Natural Science Foundation of Tianjin, China (16JCQNJC06200) for financial support.

Appendix A. Supplementary data

Supplementary data associated with this article can be found, in the online version, at http://dx.doi.org/10.1016/j.apcatb.2017.08.043.

References

[1] J. Willkomm, K.L. Orchard, A. Reynal, E. Pastor, J.R. Durrant, E. Reisner, Chem. Soc. Rev. 45 (2016) 9–23.
[2] S. Fukuzumi, Y. Yamada, T. Suenobu, K. Ohkubo, H. Kotani, Energy Environ. Sci. 4 (2011) 2754–2766.
[3] Y. Shi, B. Zhang, Chem. Soc. Rev. 45 (2016) 1529–1541.
[4] P. Mellmann, H. Junge, M. Beller, Chem. Soc. Rev. 45 (2016) 3954–3988.
[5] Y.J. Yuan, Z.T. Yu, D.Q. Chen, Z.G. Zou, Chem. Soc. Rev. 46 (2017) 603–631.
[6] X. Zou, Y. Zhang, Chem. Soc. Rev. 44 (2015) 5148–5180.
[7] Q.L. Zhu, N. Tsumori, Q. Xu, J. Am. Chem. Soc. 137 (2015) 11743–11748.
[8] N. Wang, Q. Sun, R. Bai, X. Li, G. Guo, J. Yu, J. Am. Chem. Soc. 138 (2016) 7484–7487.
[9] Q. Liu, X. Yang, Y. Huang, S. Xu, X. Su, X. Pan, J. Xu, A. Wang, C. Liang, X. Wang, T. Zhang, Energy Environ. Sci. 8 (2015) 3204–3207.
[10] M. Zacharska, L.G. Bulusheva, A.S. Lisitsyn, S. Beloshapkin, Y. Guo, A.L. Chuvilin, E.V. Shlyakhova, O.Y. Podyacheva, J.J. Leahy, A.V. Okotrub, D.A. Bulushev, ChemSusChem 10 (2017) 720–730.
[11] P. Liu, X. Gu, H. Zhang, J. Cheng, J. Song, H. Su, Appl. Catal. B 204 (2017) 497–504.
[12] J.H. Lee, J. Cho, M. Jeon, M. Ridwan, H.S. Park, S.H. Choi, S.W. Nam, J. Han, T.-H. Lim, H.C. Ham, C.W. Yoon, J. Mater. Chem. A 4 (2016) 14141–14147.
[13] D.A. Bulushev, M. Zacharska, A.S. Lisitsyn, O.Y. Podyacheva, F.S. Hage, Q.M. Ramasse, U. Bangert, L.G. Bulusheva, ACS Catal. 6 (2016) 3442–3451.
[14] A. Boddien, D. Mellmann, F. Gärtner, R. Jackstell, H. Junge, P.J. Dyson, G. Laurenczy, R. Ludwig, M. Beller, Science 333 (2011) 1733–1736.
[15] K. Fujita, R. Kawahara, T. Aikawa, R. Yamaguchi, Angew. Chem. Int. Ed. 54 (2015) 9057–9060.
[16] M. Nielsen, E. Alberico, W. Baumann, H.J. Drexler, H. Junge, S. Gladiali, M. Beller, Nature 495 (2013) 85–89.
[17] D. Bhattacharjee, S. Dasgupta, J. Mater. Chem. A 3 (2015) 24371–24378.
[18] A.M. Seayad, D.M. Antonelli, Adv. Mater. 16 (2004) 765–777.
[19] R.J. Keaton, J.M. Blacquiere, R.T. Baker, J. Am. Chem. Soc. 129 (2007) 1844–1845.
[20] P. Verma, Y. Kuwahara, K. Mori, H. Yamashita, J. Mater. Chem. A 4 (2016) 10142–10150.
[21] P. Verma, K. Yuan, Y. Kuwahara, K. Mori, H. Yamashita, Appl. Catal. B (2017), http://dx.doi.org/10.1016/j.apcatb.2017.05.017.
[22] D. Preti, S. Squarcialupi, G. Fachinetti, Angew. Chem. Int. Ed. 48 (2009) 4763–4766.

[23] H. Hu, Z. Jiao, J. Ye, G. Lu, Y. Bi, Nano Energy 8 (2014) 103–109.
[24] S. Li, H. Hu, Y. Bi, J. Mater. Chem. A 4 (2016) 796–800.
[25] R. Li, X. Zhu, X. Yan, H. Kobayashi, S. Yoshida, W. Chen, L. Du, K. Qian, B. Wu, S. Zou, L. Lu, W. Yi, Y. Zhou, J. Fan, ACS Catal. 7 (2017) 1478–1484.
[26] Y. Bi, G. Lu, Int. J. Hydrogen Energy 33 (2008) 2225–2232.
[27] P. Chowdhury, G. Malekshoar, M.B. Ray, J. Zhu, A.K. Ray, Ind. Eng. Chem. Res. 52 (2013) 5023–5029.
[28] Y. Li, T. Chen, T. Wang, Y. Zhang, G. Lu, Y. Bi, Int. J. Hydrogen Energy 39 (2014) 9114–9120.
[29] X. Pan, L. Wang, F. Ling, Y. Li, D. Han, Q. Pang, L. Jia, Int. J. Hydrogen Energy 40 (2015) 1752–1759.
[30] S. Gao, T. Feng, Q. Wu, C. Feng, N. Shang, C. Wang, RSC Adv. 6 (2016) 105638–105643.
[31] X. Pan, Z. Fan, W. Chen, Y. Ding, H. Luo, X. Bao, Nat. Mater. 6 (2007) 507–511.
[32] Y. Wan, H. Wang, Q. Zhao, M. Klingstedt, O. Terasaki, D. Zhao, J. Am. Chem. Soc. 131 (2009) 4541–4550.
[33] S. Wang, Q. Zhao, H. Wei, J.Q. Wang, M. Cho, H.S. Cho, O. Terasaki, Y. Wan, J. Am. Chem. Soc. 135 (2013) 11849–11860.
[34] Z.A. Qiao, P. Zhang, S.H. Chai, M. Chi, G.M. Veith, N.C. Gallego, M. Kidder, S. Dai, J. Am. Chem. Soc. 136 (2014) 11260–11263.
[35] X.B. Li, Y.J. Gao, Y. Wang, F. Zhan, X.Y. Zhang, Q.Y. Kong, N.J. Zhao, Q. Guo, H.L. Wu, Z.J. Li, Y. Tao, J.P. Zhang, B. Chen, C.H. Tung, L.Z. Wu, J. Am. Chem. Soc. 139 (2017) 4789–4796.
[36] W. Zhan, Q. He, X. Liu, Y. Guo, Y. Wang, L. Wang, Y. Guo, A.Y. Borisevich, J. Zhang, G. Lu, S. Dai, J. Am. Chem. Soc. 138 (2016) 16130–16139.
[37] J. Liu, K. He, W. Wu, T.B. Song, M.G. Kanatzidis, J. Am. Chem. Soc. 139 (2017) 2900–2903.
[38] Z. Qi, C. Xiao, C. Liu, T.W. Goh, L. Zhou, R. Maligal-Ganesh, Y. Pei, X. Li, L.A. Curtiss, W. Huang, J. Am. Chem. Soc. 139 (2017) 4762–4768.
[39] Q.L. Zhu, Q. Xu, Chem 1 (2016) 220–245.
[40] H. Gao, J. Zhang, R. Wang, M. Wang, Appl. Catal. B 172–173 (2015) 1–6.
[41] S. Peng, H. Peng, M. Ding, Y. Li, J. Photon. Energy 7 (2017) 016503–016514.
[42] X. Liu, X. Li, Z. Guan, J. Liu, J. Zhao, Y. Yang, Q. Yang, Chem. Commun. 47 (2011) 8073–8075.
[43] X. Liu, Y. Goto, Y. Maegawa, T. Ohsuna, S. Inagaki, APL Mater. 2 (2014) 113308–113314.
[44] S. Zhang, H. Wang, M. Li, J. Han, X. Liu, J. Gong, Chem. Sci. 8 (2017) 4489–4496.
[45] X. Zhang, F. Su, D. Song, S. An, B. Lu, Y. Guo, Appl. Catal. B 163 (2015) 50–62.
[46] D. Song, S. An, Y. Sun, Y. Guo, J. Catal. 333 (2016) 184–199.
[47] J. Sun, H. Wang, X. Gao, X. Zhu, Q. Ge, X. Liu, J. Han, Micropor. Mesopor. Mater. 247 (2017) 1–8.
[48] B.H. Wu, W.T. Liu, T.Y. Chen, T.P. Perng, J.H. Huang, L.J. Chen, Nano Energy 27 (2016) 412–419.
[49] H. Miura, K. Endo, R. Ogawa, T. Shishido, ACS Catal. 7 (2017) 1543–1553.
[50] C.H. Hao, X.N. Guo, Y.T. Pan, S. Chen, Z.F. Jiao, Hong Yang, X.Y. Guo, J. Am. Chem. Soc. 138 (2016) 9361–9364.
[51] R. Long, Y. Li, Y. Liu, S. Chen, X. Zheng, C. Gao, C. He, N. Chen, Z. Qi, L. Song, J. Jiang, J. Zhu, Y. Xiong, J. Am. Chem. Soc. 139 (2017) 4486–4492.
[52] C. Kim, B.L. Suh, H. Yun, J. Kim, H. Lee, ACS Catal. 7 (2017) 2294–2302.
[53] Y. Ding, W. Sun, W. Yang, Q. Li, Appl. Catal. B 203 (2017) 372–380.
[54] L. Xu, F. Yao, J. Luo, C. Wan, M. Ye, P. Cui, Y. An, RSC Adv. 7 (2017) 4746–4752.
[55] M. Yurderi, A. Bulut, N. Caner, M. Celebi, M. Kaya, M. Zahmakiran, Chem. Commun. 51 (2015) 11417–11420.
[56] Z. Li, X. Yang, N. Tsumori, Z. Liu, Y. Himeda, T. Autrey, Q. Xu, ACS Catal. 7 (2017) 2720–2724.
[57] H. Miyamura, R. Matsubara, Y. Miyazaki, S. Kobayashi, Angew. Chem. Int. Ed. 119 (2007) 4229–4232.
[58] M. Seo, D.W. Lee, S.S. Han, K.Y. Lee, ACS Catal. 7 (2017) 3039–3048.
[59] F. Wang, J. Xu, X. Shao, X. Su, Y. Huang, T. Zhang, ChemSusChem 9 (2016) 246–251.
[60] F. Jiang, R. Li, J. Cai, W. Xu, A. Cao, D. Chen, X. Zhang, C. Wang, C. Shu, J. Mater. Chem. A 3 (2015) 19433–19438.
[61] P. Christopher, H. Xin, S. Linic, Nat. Chem 3 (2011) 467–472.
[62] M. Wen, K. Mori, Y. Kuwahara, H. Yamashita, ACS Energy Lett. 2 (2017) 1–7.